Differential near-edge coherent diffractive imaging using a femtosecond high-harmonic XUV light source

Fabian Weise,[1] Daniel M. Neumark,[1,2] Stephen R. Leone,[1,2,3] and Oliver Gessner[1,*]

[1]*Ultrafast X-ray Science Laboratory, Chemical Sciences Division, Lawrence Berkeley National Laboratory, Berkeley, California 94720, USA*
[2]*Department of Chemistry, University of California, Berkeley, California 94720, USA*
[3]*Department of Physics, University of California, Berkeley, California 94720, USA*
**ogessner@lbl.gov*

Abstract: Element-specific contrast enhancement in tabletop coherent diffractive imaging (CDI) is demonstrated by employing an ultrafast extreme ultraviolet (XUV) light source with tunable photon energy. By combining two measurements performed at energies below and above the Al $L_{2,3}$ absorption edge, the spatial autocorrelation function of a micron-scale double pinhole in a 300 nm thick aluminum foil is retrieved despite a dominant background signal from directly transmitted light across the entire range of detectable diffraction angles. The fringe visibility in the diffraction patterns is 0 below the Al $L_{2,3}$ edge, 0.53 ± 0.06 above the edge, and 0.73 ± 0.08 in the differential image that combines the two measurements. The proof-of-principle experiment demonstrates that the variations of XUV optical constants in the vicinity of an inner-shell absorption edge can be utilized to improve the chemical sensitivity and image reconstruction quality of laboratory-based ultrafast imaging experiments.

OCIS codes: (110.7440) X-ray imaging; (340.7480) X-rays, soft X-rays, extreme ultraviolet (EUV); (190.2620) Harmonic generation and mixing.

References and links

1. A. Sakdinawat and D. Attwood, "Nanoscale X-ray imaging," Nat. Photonics **4**(12), 840–848 (2010).
2. D. Sayre, "Prospects for long-wavelength X-ray microscopy and diffraction," in *Imaging Processes and Coherence in Physics*, M. Schlenker, M. Fink, J. Goedgebuer, C. Malgrange, J. Vieénot, and R. Wade, eds. (Springer Berlin / Heidelberg, 1980), pp. 229–235.
3. J. Miao, P. Charalambous, J. Kirz, and D. Sayre, "Extending the methodology of X-ray crystallography to allow imaging of micrometre-sized non-crystalline specimens," Nature **400**(6742), 342–344 (1999).
4. M. J. Bogan, W. H. Benner, S. Boutet, U. Rohner, M. Frank, A. Barty, M. M. Seibert, F. Maia, S. Marchesini, S. Bajt, B. Woods, V. Riot, S. P. Hau-Riege, M. Svenda, E. Marklund, E. Spiller, J. Hajdu, and H. N. Chapman, "Single particle X-ray diffractive imaging," Nano Lett. **8**(1), 310–316 (2008).
5. X. Huang, J. Nelson, J. Kirz, E. Lima, S. Marchesini, H. Miao, A. M. Neiman, D. Shapiro, J. Steinbrener, A. Stewart, J. J. Turner, and C. Jacobsen, "Soft X-ray diffraction microscopy of a frozen hydrated yeast cell," Phys. Rev. Lett. **103**(19), 198101 (2009).
6. S. Eisebitt, J. Lüning, W. F. Schlotter, M. Lörgen, O. Hellwig, W. Eberhardt, and J. Stöhr, "Lensless imaging of magnetic nanostructures by X-ray spectro-holography," Nature **432**(7019), 885–888 (2004).
7. S. Roy, D. Parks, K. A. Seu, R. Su, J. J. Turner, W. Chao, E. H. Anderson, S. Cabrini, and S. D. Kevan, "Lensless X-ray imaging in reflection geometry," Nat. Photonics **5**(4), 243–245 (2011).
8. H. N. Chapman, A. Barty, M. J. Bogan, S. Boutet, M. Frank, S. P. Hau-Riege, S. Marchesini, B. W. Woods, S. Bajt, W. H. Benner, R. A. London, E. Plönjes, M. Kuhlmann, R. Treusch, S. Düsterer, T. Tschentscher, J. R. Schneider, E. Spiller, T. Möller, C. Bostedt, M. Hoener, D. A. Shapiro, K. O. Hodgson, D. van der Spoel, F. Burmeister, M. Bergh, C. Caleman, G. Huldt, M. M. Seibert, F. R. N. C. Maia, R. W. Lee, A. Szöke, N. Timneanu, and J. Hajdu, "Femtosecond diffractive imaging with a soft-X-ray free-electron laser," Nat. Phys. **2**(12), 839–843 (2006).
9. M. M. Seibert, T. Ekeberg, F. R. N. C. Maia, M. Svenda, J. Andreasson, O. Jönsson, D. Odić, B. Iwan, A. Rocker, D. Westphal, M. Hantke, D. P. DePonte, A. Barty, J. Schulz, L. Gumprecht, N. Coppola, A. Aquila, M. Liang, T. A. White, A. Martin, C. Caleman, S. Stern, C. Abergel, V. Seltzer, J.-M. Claverie, C. Bostedt, J. D.

#174995 - $15.00 USD Received 27 Aug 2012; revised 19 Oct 2012; accepted 21 Oct 2012; published 5 Nov 2012

Bozek, S. Boutet, A. A. Miahnahri, M. Messerschmidt, J. Krzywinski, G. Williams, K. O. Hodgson, M. J. Bogan, C. Y. Hampton, R. G. Sierra, D. Starodub, I. Andersson, S. Bajt, M. Barthelmess, J. C. H. Spence, P. Fromme, U. Weierstall, R. Kirian, M. Hunter, R. B. Doak, S. Marchesini, S. P. Hau-Riege, M. Frank, R. L. Shoeman, L. Lomb, S. W. Epp, R. Hartmann, D. Rolles, A. Rudenko, C. Schmidt, L. Foucar, N. Kimmel, P. Holl, B. Rudek, B. Erk, A. Hömke, C. Reich, D. Pietschner, G. Weidenspointner, L. Strüder, G. Hauser, H. Gorke, J. Ullrich, I. Schlichting, S. Herrmann, G. Schaller, F. Schopper, H. Soltau, K.-U. Kühnel, R. Andritschke, C.-D. Schröter, F. Krasniqi, M. Bott, S. Schorb, D. Rupp, M. Adolph, T. Gorkhover, H. Hirsemann, G. Potdevin, H. Graafsma, B. Nilsson, H. N. Chapman, and J. Hajdu, "Single mimivirus particles intercepted and imaged with an X-ray laser," Nature **470**(7332), 78–81 (2011).

10. H. N. Chapman, P. Fromme, A. Barty, T. A. White, R. A. Kirian, A. Aquila, M. S. Hunter, J. Schulz, D. P. DePonte, U. Weierstall, R. B. Doak, F. R. N. C. Maia, A. V. Martin, I. Schlichting, L. Lomb, N. Coppola, R. L. Shoeman, S. W. Epp, R. Hartmann, D. Rolles, A. Rudenko, L. Foucar, N. Kimmel, G. Weidenspointner, P. Holl, M. Liang, M. Barthelmess, C. Caleman, S. Boutet, M. J. Bogan, J. Krzywinski, C. Bostedt, S. Bajt, L. Gumprecht, B. Rudek, B. Erk, C. Schmidt, A. Hömke, C. Reich, D. Pietschner, L. Strüder, G. Hauser, H. Gorke, J. Ullrich, S. Herrmann, G. Schaller, F. Schopper, H. Soltau, K.-U. Kühnel, M. Messerschmidt, J. D. Bozek, S. P. Hau-Riege, M. Frank, C. Y. Hampton, R. G. Sierra, D. Starodub, G. J. Williams, J. Hajdu, N. Timneanu, M. M. Seibert, J. Andreasson, A. Rocker, O. Jönsson, M. Svenda, S. Stern, K. Nass, R. Andritschke, C.-D. Schröter, F. Krasniqi, M. Bott, K. E. Schmidt, X. Wang, I. Grotjohann, J. M. Holton, T. R. M. Barends, R. Neutze, S. Marchesini, R. Fromme, S. Schorb, D. Rupp, M. Adolph, T. Gorkhover, I. Andersson, H. Hirsemann, G. Potdevin, H. Graafsma, B. Nilsson, and J. C. H. Spence, "Femtosecond X-ray protein nanocrystallography," Nature **470**(7332), 73–77 (2011).
11. N. D. Loh, C. Y. Hampton, A. V. Martin, D. Starodub, R. G. Sierra, A. Barty, A. Aquila, J. Schulz, L. Lomb, J. Steinbrener, R. L. Shoeman, S. Kassemeyer, C. Bostedt, J. Bozek, S. W. Epp, B. Erk, R. Hartmann, D. Rolles, A. Rudenko, B. Rudek, L. Foucar, N. Kimmel, G. Weidenspointner, G. Hauser, P. Holl, E. Pedersoli, M. Liang, M. S. Hunter, L. Gumprecht, N. Coppola, C. Wunderer, H. Graafsma, F. R. N. C. Maia, T. Ekeberg, M. Hantke, H. Fleckenstein, H. Hirsemann, K. Nass, T. A. White, H. J. Tobias, G. R. Farquar, W. H. Benner, S. P. Hau-Riege, C. Reich, A. Hartmann, H. Soltau, S. Marchesini, S. Bajt, M. Barthelmess, P. Bucksbaum, K. O. Hodgson, L. Strüder, J. Ullrich, M. Frank, I. Schlichting, H. N. Chapman, and M. J. Bogan, "Fractal morphology, imaging and mass spectrometry of single aerosol particles in flight," Nature **486**(7404), 513–517 (2012).
12. S. Boutet, L. Lomb, G. J. Williams, T. R. M. Barends, A. Aquila, R. B. Doak, U. Weierstall, D. P. DePonte, J. Steinbrener, R. L. Shoeman, M. Messerschmidt, A. Barty, T. A. White, S. Kassemeyer, R. A. Kirian, M. M. Seibert, P. A. Montanez, C. Kenney, R. Herbst, P. Hart, J. Pines, G. Haller, S. M. Gruner, H. T. Philipp, M. W. Tate, M. Hromalik, L. J. Koerner, N. van Bakel, J. Morse, W. Ghonsalves, D. Arnlund, M. J. Bogan, C. Caleman, R. Fromme, C. Y. Hampton, M. S. Hunter, L. C. Johansson, G. Katona, C. Kupitz, M. Liang, A. V. Martin, K. Nass, L. Redecke, F. Stellato, N. Timneanu, D. Wang, N. A. Zatsepin, D. Schafer, J. Defever, R. Neutze, P. Fromme, J. C. H. Spence, H. N. Chapman, and I. Schlichting, "High-resolution protein structure determination by serial femtosecond crystallography," Science **337**(6092), 362–364 (2012).
13. R. L. Sandberg, A. Paul, D. A. Raymondson, S. Hädrich, D. M. Gaudiosi, J. Holtsnider, R. I. Tobey, O. Cohen, M. M. Murnane, H. C. Kapteyn, C. Song, J. Miao, Y. Liu, and F. Salmassi, "Lensless diffractive imaging using tabletop coherent high-harmonic soft-X-ray beams," Phys. Rev. Lett. **99**(9), 098103 (2007).
14. M. D. Seaberg, D. E. Adams, E. L. Townsend, D. A. Raymondson, W. F. Schlotter, Y. Liu, C. S. Menoni, L. Rong, C.-C. Chen, J. Miao, H. C. Kapteyn, and M. M. Murnane, "Ultrahigh 22 nm resolution coherent diffractive imaging using a desktop 13 nm high harmonic source," Opt. Express **19**(23), 22470–22479 (2011).
15. R. L. Sandberg, C. Song, P. W. Wachulak, D. A. Raymondson, A. Paul, B. Amirbekian, E. Lee, A. E. Sakdinawat, C. La-O-Vorakiat, M. C. Marconi, C. S. Menoni, M. M. Murnane, J. J. Rocca, H. C. Kapteyn, and J. Miao, "High numerical aperture tabletop soft x-ray diffraction microscopy with 70-nm resolution," Proc. Natl. Acad. Sci. U.S.A. **105**(1), 24–27 (2008).
16. A. Ravasio, D. Gauthier, F. R. N. C. Maia, M. Billon, J. P. Caumes, D. Garzella, M. Géléoc, O. Gobert, J. F. Hergott, A. M. Pena, H. Perez, B. Carré, E. Bourhis, J. Gierak, A. Madouri, D. Mailly, B. Schiedt, M. Fajardo, J. Gautier, P. Zeitoun, P. H. Bucksbaum, J. Hajdu, and H. Merdji, "Single-shot diffractive imaging with a table-top femtosecond soft x-ray laser-harmonics source," Phys. Rev. Lett. **103**(2), 028104 (2009).
17. D. Gauthier, M. Guizar-Sicairos, X. Ge, W. Boutu, B. Carré, J. R. Fienup, and H. Merdji, "Single-shot femtosecond x-ray holography using extended references," Phys. Rev. Lett. **105**(9), 093901 (2010).
18. T. Ditmire, E. T. Gumbrell, R. A. Smith, J. W. G. Tisch, D. D. Meyerhofer, and M. H. R. Hutchinson, "Spatial coherence measurement of soft X-ray radiation produced by high order harmonic generation," Phys. Rev. Lett. **77**(23), 4756–4759 (1996).
19. C. Song, R. Bergstrom, D. Ramunno-Johnson, H. Jiang, D. Paterson, M. D. de Jonge, I. McNulty, J. Lee, K. L. Wang, and J. Miao, "Nanoscale imaging of buried structures with elemental specificity using resonant x-ray diffraction microscopy," Phys. Rev. Lett. **100**(2), 025504 (2008).
20. A. Scherz, D. Zhu, R. Rick, W. F. Schlotter, S. Roy, J. Lüning, and J. Stöhr, "Nanoscale imaging with resonant coherent X rays: extension of multiple-wavelength anomalous diffraction to nonperiodic structures," Phys. Rev. Lett. **101**(7), 076101 (2008).
21. M. Beckers, T. Senkbeil, T. Gorniak, M. Reese, K. Giewekemeyer, S.-C. Gleber, T. Salditt, and A. Rosenhahn, "Chemical contrast in soft x-ray ptychography," Phys. Rev. Lett. **107**(20), 208101 (2011).
22. F. Weise, D. M. Neumark, S. R. Leone, and O. Gessner, In Preparation.

#174995 - $15.00 USD Received 27 Aug 2012; revised 19 Oct 2012; accepted 21 Oct 2012; published 5 Nov 2012

23. Y. Nagata, Y. Nabekawa, and K. Midorikawa, "Development of high-throughput, high-damage-threshold beam separator for 13 nm high-order harmonics," Opt. Lett. **31**(9), 1316–1318 (2006).
24. B. L. Henke, E. M. Gullikson, and J. C. Davis, "X-ray interactions: photoabsorption, scattering, transmission, and reflection at E = 50-30,000 eV, Z = 1-92," At. Data Nucl. Data Tables **54**(2), 181–342 (1993).
25. J. C. H. Spence, U. Weierstall, and M. Howells, "Coherence and sampling requirements for diffractive imaging," Ultramicroscopy **101**(2-4), 149–152 (2004).
26. S. Billinge, "The nanostructure problem," Physics **3**, 25 (2010).
27. J. Miao, J. Kirz, and D. Sayre, "The oversampling phasing method," Acta Crystallogr. Sect D: Biol. Crystallogr. **56**(10), 1312–1315 (2000).
28. S. Marchesini, H. He, H. N. Chapman, S. P. Hau-Riege, A. Noy, M. R. Howells, U. Weierstall, and J. C. H. Spence, "X-ray image reconstruction from a diffraction pattern alone," Phys. Rev. B Condens. Matter **68**(14), 140101 (2003).
29. S. Marchesini, "Invited article: a [corrected] unified evaluation of iterative projection algorithms for phase retrieval," Rev. Sci. Instrum. **78**(1), 011301 (2007).
30. S. Marchesini, "Ab initio compressive phase retrieval," arXiv:0809.2006 (2008).

1. Introduction

Microscopy is one of the most fundamental tools to study the structure of matter and to understand the relationship between structural properties and function. X-ray based microscopy can in principle reveal structural details on the sub-nanometer scale, holding great promise for a new level of insight into the fundamental properties of engineered nano-structures, macromolecular building blocks of living organisms, and even single molecules on their natural length scales [1]. Lensless imaging in which an X-ray detector records the diffraction pattern that is generated by the coherent superposition of light scattered from different moieties of a sample is increasingly attracting attention [2–17]. This approach is adapted from crystallography and has been extended to imaging of non-periodic samples. Despite the lack of direct phase information in the recorded intensities, real-space images can be reconstructed by combining spatial oversampling of the diffraction patterns with iterative phase retrieval algorithms. Coherent diffractive imaging (CDI) of periodic and non-periodic samples has been successfully demonstrated using synchrotron radiation light sources [5–7], free electron lasers (FELs) [8–12], and tabletop ultrafast extreme ultraviolet (XUV) light sources [13–17]. Here, a tabletop CDI study is presented that employs an XUV light source with tunable photon energies to enhance the element-specific contrast (fringe visibility) in the recorded diffraction patterns.

CDI with XUV light pulses generated by high-harmonic generation (HHG) is of particular interest owing to its potential to perform time-resolved CDI measurements in a laboratory-based environment. Studies by Ditmire et al. [18] demonstrated that picosecond XUV light pulses produced by HHG exhibit a significant degree of spatial coherence. More recently, femtosecond HHG light sources have been employed by the groups of Kapteyn and Murnane [13,14], Miao [15] and Merdji [16,17] to perform multi- and single-shot CDI studies. These experiments beautifully demonstrate faithful real-space image reconstructions with up to near diffraction limited spatial resolution.

In addition to providing superb spatial resolution, XUV- and X-ray light sources can exploit the known variations of optical constants in the vicinity of element-specific inner-shell absorption edges for imaging purposes. Synchrotron-based CDI studies routinely use the abrupt change in the absorption cross section and scattering phase to gain chemical contrast and to improve image reconstruction quality [19–21]. In this paper, a method is presented that extends these ideas to tabletop CDI experiments. Differential near-edge CDI is based on two independent measurements below and above an element-specific inner shell absorption edge. The difference between the recorded images is inherently sensitive to a specific chemical species. The advantage of the method is demonstrated by extracting the spatial autocorrelation function of a micron-scale double pinhole in a 300 nm thick aluminum foil. We envision that this proof-of-principle experiment opens new possibilities for ultrafast imaging applications by enabling chemical contrast and enhancing the reliability of image

#174995 - $15.00 USD Received 27 Aug 2012; revised 19 Oct 2012; accepted 21 Oct 2012; published 5 Nov 2012

reconstruction algorithms in challenging situations where only a small fraction of the incoming light is scattered by the sample features of interest.

2. Experiment

A schematic of the experimental setup is shown in Fig. 1(a). A detailed description of the apparatus will be given elsewhere [22]. Briefly, ultrashort XUV pulses are produced by focusing the output of a Ti:Sapphire based femtosecond laser system into a 50 mm long gas cell filled with neon gas at a stagnation pressure of 8 Torr. The laser system is operated at 3 kHz repetition rate, a pulse energy of 4.5 mJ, and a center wavelength of 785 nm. The femtosecond XUV pulses produced by HHG are separated from the co-propagating infrared driver pulses by a dichroic mirror based on a NbN coated silicon substrate [23]. XUV pulses with quasi-continuously tunable energies are focused onto the sample by a monochromator that consists of a toroidal mirror and a plane grating with constant line spacing (600 lines/mm). The energy resolution at 71.2 eV and 74.4 eV, corresponding to the maxima of the 45th and 47th harmonics, respectively, is 0.39 eV (FWHM) [22]. At the peak of these harmonics the photon fluence on target is ~10^5 photons/pulse/1 eV bandwidth.

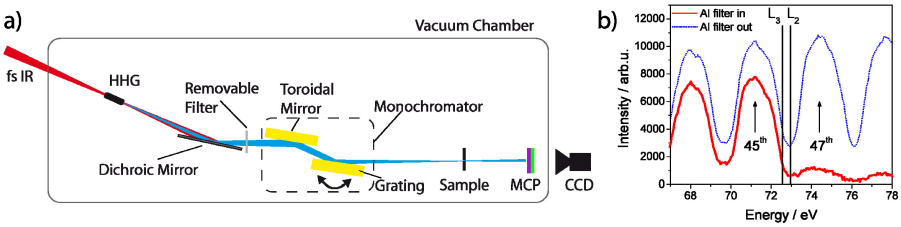

Fig. 1. (a) Experimental setup for energy-resolved tabletop coherent diffractive imaging. (b) High harmonic spectra in the vicinity of the aluminum $L_{2,3}$-edges, which are indicated by two vertical lines. The red solid curve is recorded with an optional aluminum filter placed in between the dichroic mirror and the monochromator. The two photon energies used in this study are indicated by arrows.

The single-grating monochromator design leads to a temporal broadening of the XUV pulses that is proportional to the number of illuminated grooves on the grating. For energies in the vicinity of the Al L-edges, the estimated pulse length at the monochromator exit is ~650 fs.

Light transmitted through the sample is detected by means of a microchannel plate (MCP) imaging detector equipped with a phosphor screen. The screen is imaged onto a CCD camera that is mounted outside the vacuum system. Harmonic spectra are recorded by removing the sample and placing the imaging detector near the focusing surface of the monochromator. Figure 1(b) shows high harmonic spectra recorded with (solid red) and without (dotted blue) a 200 nm thick Al filter in the beam path between the dichroic mirror and the monochromator. The spectral intensity beyond the Al $L_{2,3}$ absorption edges (~73 eV) is strongly suppressed by the filter; the measured transmission at 74.4 eV is ~11%. This value is greater than the theoretical estimate of ~2.4% [24], which is probably due to imperfections, such as pinholes, in the thin Al foil, and the contribution of scattered XUV light with photon energies below the absorption edges. The well known energies of the Al $L_{2,3}$ absorption edges [24] facilitate a straightforward identification of the harmonic orders and an absolute energy calibration of the setup. The spatial coherence of the XUV wavefront at the sample is approximately 88 ± 3% as determined by a double-slit measurement [22].

In the work presented here, the sample consists of a 300 nm thick aluminum foil that is placed across a circular aperture of 150 µm diameter (Fig. 2(a)). The aperture is made of a 13 µm thick stainless steel foil, which is opaque for the XUV light used in this experiment. Two 5 µm wide, 20 µm spaced holes are laser-drilled into the center of the aluminum foil. Figure 2(b) shows a scanning electron microscope (SEM) image of the two pinholes (black).

#174995 - $15.00 USD Received 27 Aug 2012; revised 19 Oct 2012; accepted 21 Oct 2012; published 5 Nov 2012

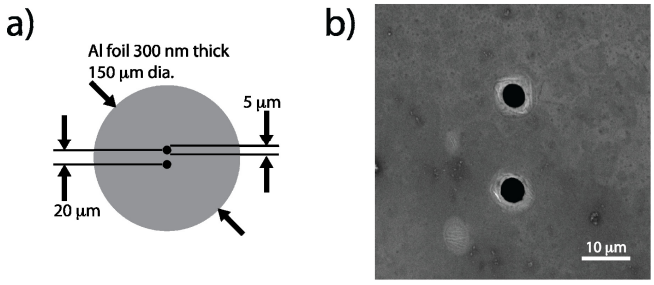

Fig. 2. (a) Schematic of the test sample. Two 5 μm pinholes are laser drilled into a 300 nm thick Aluminum foil that is supported by an opaque 150 μm aperture. (b) Scanning electron microscope image of the central part of the sample. The two black areas are the pinholes in the aluminum foil, which is shown in gray.

By selecting either the 45th or the 47th harmonic, images are recorded at photon energies of 71.2 eV or 74.4 eV, approximately 1.6 eV below and above the aluminum $L_{2,3}$ absorption edges, respectively. The theoretical transmission of a 300 nm thick aluminum foil at 71.2 eV and 74.4 eV is 0.63 and $3.7 \cdot 10^{-3}$, respectively [24]. Note, however, that due to the large ratio between the areas of the stainless steel aperture and the pinholes, the number of detected photons that pass through the Al foil is expected to exceed the number of photons passing through the pinholes by a factor of ~280 and ~2 for the 45th and 47th harmonic, respectively. Each diffraction pattern is accumulated for 200 s, corresponding to $6x10^5$ laser pulses. The signal background from scattered IR light is recorded by removing the gas from the HHG cell. This background is measured and subtracted individually for each single data set.

3. Photon energy dependent diffraction images

Figures 3(a) and 3(b) show images recorded at 71.2 eV and 74.4 eV photon energies, respectively. The energy bandwidth in both cases is 0.39 eV (FWHM). The pattern in Fig. 3(b) is recorded at higher MCP voltages than the pattern in Fig. 3(a) to compensate for the higher XUV photon absorption in the sample at energies above the Al $L_{2,3}$ edges. At first glance, neither image bears any signature of the double hole structure in the center of the sample. The elongated peaks, which are very similar for both photon energies, represent the geometrical projection of the XUV beam onto the imaging detector after passing through the 150 μm aperture in the stainless steel foil. Diffraction effects due to this aperture can be neglected since its diameter is much larger than the wavelength of the XUV light (~17 nm). The peaks are elongated due to the astigmatic focusing geometry of the monochromator. The difference in the horizontal elongation of the two peaks is due to the chromatic aberration in the monochromator.

Figure 3(c) shows the intensity distributions for 71.2 eV (green dashed) and 74.4 eV (red solid) along the vertical axis that connects the two holes in the sample after integration of the images along the horizontal axis. The two curves are normalized to the same integrated intensity in the central peak. A slight difference between the two patterns can be discerned in the pedestal of the central main feature. The difference appears more clearly in the magnified pedestal region shown in Fig. 3(d). While the intensity in the image recorded at 71.2 eV falls off monotonically with increasing distance from the center, the image recorded at 74.4 eV exhibits additional structure. This structure can be attributed to diffraction from the double pinhole that becomes detectable upon tuning the photon energy above the Al $L_{2,3}$ edges.

#174995 - $15.00 USD Received 27 Aug 2012; revised 19 Oct 2012; accepted 21 Oct 2012; published 5 Nov 2012

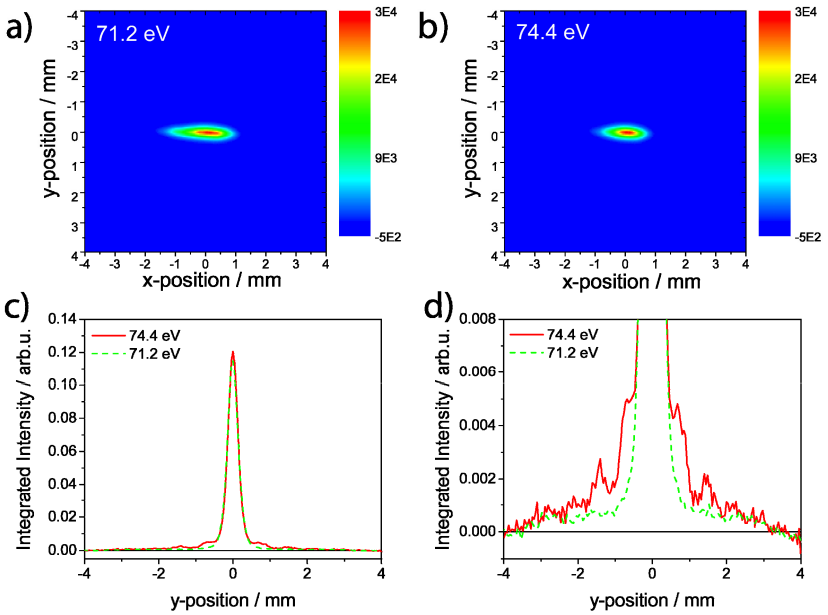

Fig. 3. Diffraction patterns recorded with photon energies of (a) 71.2 eV and (b) 74.4 eV, closely below and above the aluminum $L_{2,3}$-edges, respectively. (c) Diffraction patterns after integration along the horizontal axis and normalization to the same intensity in the dominant center peak. (d) Magnified pedestal region of (c).

Generally, each image is a superposition of the geometrical projection of the 150 µm aperture and the diffraction pattern of the double pinhole. Both images are clearly dominated by the former as illustrated in Figs. 3(a)-3(c). At 71.2 eV, the number of photons passing through the double pinhole is negligible compared to the total number of photons reaching the detector. Correspondingly, the green dashed curves in Figs. 3(c), 3(d) do not show any indications of the pinhole structure. At 74.4 eV, however, the ratio of detected photons that pass through the double pinhole and through the Al foil is about 1:6, making the diffraction features of the pinholes discernible as oscillating structure on top of the directly transmitted signal. The measured ratio may be lower than expected (~1:2) due to contributions from scattered XUV light with different wavelengths and small imperfections in the Al foil.

Figure 4(a) shows the difference between the images recorded at 74.4 eV and 71.2 eV after normalizing the intensities with the same scaling factor as used to generate Fig. 3(c). In contrast to Figs. 3(a) and 3(b), the features of a double pinhole diffraction pattern are readily apparent, in agreement with a simulation (Fig. 4(b)) based on the SEM image of the sample (Fig. 2(b)). The quantitative agreement between experiment and simulation is illustrated in Fig. 4(c), which shows the simulated (blue curve) and measured (orange squares) diffraction intensities after integration of the images along the horizontal axis. The center portions of Figs. 4(a), 4(c) exhibit some artifacts that are caused by the chromatic aberration effects described above. Even slight differences between the wavelength dependent geometrical projections of the 150 µm aperture have a significant impact in this region, where the intensity of the non-diffracted light exceeds the diffracted intensity by approximately one order of magnitude. Nevertheless, the differential near-edge imaging method retrieves the major portion of the double pinhole diffraction pattern.

#174995 - $15.00 USD Received 27 Aug 2012; revised 19 Oct 2012; accepted 21 Oct 2012; published 5 Nov 2012

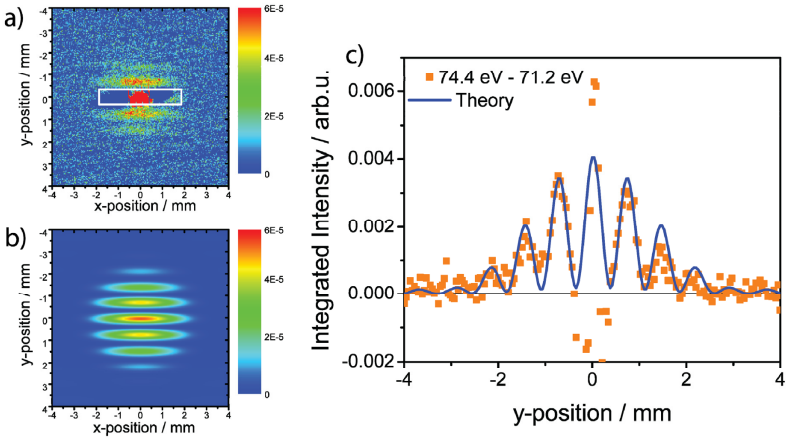

Fig. 4. (a) Difference of the normalized diffraction patterns recorded at 74.4 eV and 71.2 eV. (b) Simulated double pinhole diffraction pattern for 74.4 eV photon energy. (c) Differential CDI signal from (a) (squares) and calculated double pinhole diffraction pattern (b) (solid line) after integration along the horizontal axis.

The fringe visibility, defined as the contrast between neighboring maxima and minima in the diffraction pattern C = (max-min)/(max + min), is a measure for the contrast improvement provided by the differential CDI measurement. For the two data sets recorded at 71.2 eV and 74.4 eV, and the differential signal, the fringe contrasts are 0, 0.53 ± 0.06, and 0.73 ± 0.08, respectively. The fringe contrast is not affected by the finite energy resolution of the monochromator. The energy resolution of 0.39 eV (FWHM) at 73 eV photon energy translates into a variation of the wavelength of less than 1%, which has negligible impact on the results presented here. Note that lowering the photon energy from above to below the Al $L_{2,3}$-edges effectively mimics the removal of the Al foil from the beam path. Thus, differential near-edge CDI provides direct access to element specific diffractive images.

4. Reconstructed spatial autocorrelation functions

In this section, the spatial autocorrelation function of the target is derived from a) the two-dimensional Fourier transform (FT) of the diffraction patterns and b) the spatial autocorrelation function of the SEM image. In principle, the results should be identical [25,26]. The comparison of the spatial autocorrelation functions obtained by these two complementary methods is used to assess the real-space information that may be gained from the diffraction patterns.

We define the spatial autocorrelation function *A(x,y)* of the double pinhole structure as

$$A(x,y) = \int_{-100\,\mu m}^{100\,\mu m} O(x,y)O(x-p,y-q)\,dpdq \qquad (1)$$

Here, *O(x,y)* is a binary intensity distribution representing the two-dimensional sample. *O(x,y)* is 1 for positions *(x,y)* within one of the pinholes and 0 for all other positions.

Generally, the retrieval of autocorrelation functions from measured data by FT techniques requires accounting for the influence of experimental effects such as noise, partially missing image sections, and a finite sample support. The art of retrieving real-space information from diffraction images is a topic of intense research [27–29], which we only cite in this context without further discussion.

Here, an iterative 2D-FT algorithm based on the work of Marchesini [30] is applied to reconstruct the two-dimensional spatial autocorrelation function from the measured diffraction pattern. Before applying the algorithm, the central part of the image marked by a white rectangle in Fig. 4(a) is set to zero to minimize the impact of the artifacts described

#174995 - $15.00 USD Received 27 Aug 2012; revised 19 Oct 2012; accepted 21 Oct 2012; published 5 Nov 2012

above. The impact of this "virtual beam block" on the spatial autocorrelation function is greatly reduced by the algorithm that effectively optimizes a self-consistent 2D-FT correlation between a baseline-corrected real-space image and a modified reciprocal space image. In the latter, the zone within the white rectangle in Fig. 4(a) is replaced by the corresponding zone of the inverse 2D-FT of the baseline-corrected real space image.

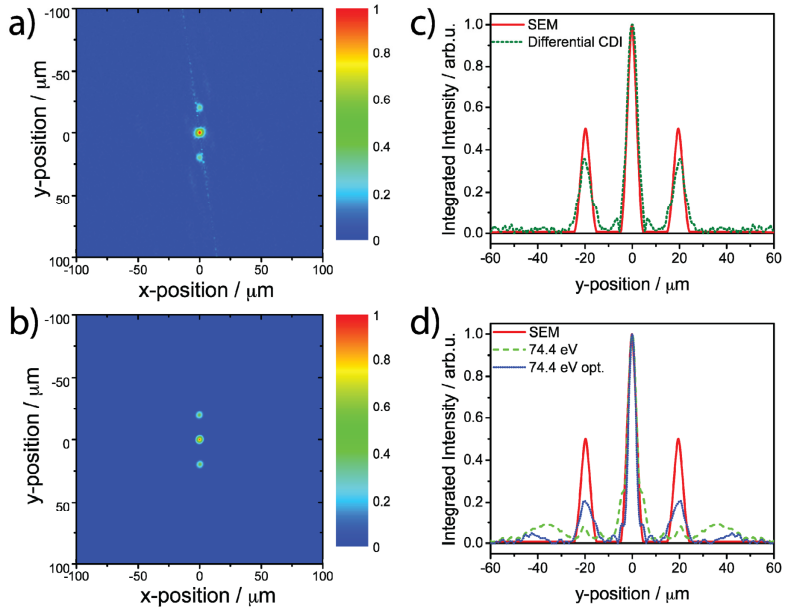

Fig. 5. Spatial autocorrelation functions of the double pinhole sample (a) reconstructed from the differential CDI signal and (b) calculated from the SEM image. (c) Vertical line-outs of (a) (green dotted) and (b) (red solid). (d) Vertical line-outs of autocorrelation functions calculated from SEM image (solid) and reconstructed from single photon energy measurements. The green dashed curve is generated by applying the same reconstruction procedure as for the differential CDI signal in Figs. 5(a), 5(c). The blue dotted curve is generated by optimizing the reconstruction procedure for best possible agreement between the measured and the calculated autocorrelation functions using image data recorded at 74.4 eV.

The result of this optimization procedure is shown in Fig. 5(a). It shows three horizontally centered peaks that should correspond to the spatial autocorrelation function of a double pinhole with the holes on a common vertical axis. For comparison, Fig. 5(b) shows the spatial autocorrelation function derived from applying Eq. (1) to the SEM image in Fig. 2(b). The quantitative agreement between the main features in Fig. 5(a) and Fig. 5(b) is illustrated in Fig. 5(c), which displays vertical line-outs along the center (x = 0) of the measured (dashed) and simulated (solid) autocorrelation functions. The theoretical peak positions, peak widths and relative peak intensities are well reproduced by the experimental data. More precisely, the autocorrelation function derived by differential near-edge imaging corresponds to a hole separation of 19.86 ± 0.03 µm and a hole diameter of 5.27 ± 0.06 µm while the SEM image analysis leads to a hole separation of 19.6 ± 0.3 µm and a hole diameter of 4.9 ± 0.3 µm. We note that this excellent agreement is partly due to the simple structure of the sample. The theoretical resolution limit derived from the maximum scattering angle at which signals can be discerned from the background is approximately 4 µm. The resolution is predominantly defined by the rather poor signal-to-noise ratio of the home-built X-ray imaging detector, which severely limits the range of usable scattering angles.

Note that the thin line that crosses the measured autocorrelation function at an angle of 8° is not an artifact caused by the image inversion algorithm. The angle coincides with the experimental tilt angle between the camera and the double pinhole structure, indicating that

#174995 - $15.00 USD Received 27 Aug 2012; revised 19 Oct 2012; accepted 21 Oct 2012; published 5 Nov 2012

the response of the CCD camera may be causing the line to appear. In the future, a dedicated commercial X-ray camera and an achromatic monochromator configuration will significantly improve the overall performance of the setup. However, the fact that the differential measurement leads to a reasonable reconstruction of the spatial autocorrelation function despite the experimental limitations indicates that differential CDI provides a robust, reliable mechanism to access element-specific image information under challenging conditions.

The advantage of using differential near-edge CDI compared to a single measurement at a photon energy just above the absorption edge is demonstrated in Fig. 5(d). The solid line corresponds to a vertical line-out through the center (x = 0) of the theoretical autocorrelation function based on the SEM image. The green dashed line is the result of analyzing the 2D FT of the diffraction pattern recorded at 74.4 eV (Fig. 3(b)) in the same way as the 2D FT of the differential image (Figs. 4(a), 5(c)) including the application of the same virtual beam block marked by the white rectangle in Fig. 4(a). This autocorrelation function is entirely dominated by a single center peak and information about the double pinhole structure of the sample is mostly lost in the broad side features. The blue dotted line in Fig. 5(d) was generated by optimizing the size of the virtual beam block to achieve the best agreement between the measured and the theoretical autocorrelation functions. Even when guiding the image analysis in this way, which effectively makes use of complete knowledge of the sample structure, the intensity ratio between the center and the side peaks differs from the theoretically expected ratio by 50% as opposed to a deviation of 27% for the differential CDI results. Clearly, when there is significant spatial overlap of diffracted and non-diffracted signals, the differential near-edge imaging method is much better suited to suppress the impact of the non-diffracted light contributions on the image reconstruction than the application of a beam block at a single photon energy. We note that in some situations, differential near-edge CDI may also aid phase retrieval during real-space reconstruction procedures as demonstrated, for example, in the synchrotron-based study by Stöhr and associates [20].

5. Conclusion and outlook

A method to enhance the element-specific contrast and image reconstruction quality in ultrafast tabletop CDI experiments is presented. By employing the variations of XUV optical constants in the vicinity of the Al $L_{2,3}$ inner-shell absorption edges, the spatial autocorrelation function of a micron-scale double pinhole in a partially transparent Al foil is reconstructed despite the dominant contribution of non-diffracted light in the recorded image. It is shown that the differential measurement provides a more faithful autocorrelation function of the sample than the suppression of zero-order diffraction components by an optimized beam block. The proof-of-principle experiment is a first step toward the goal of translating the unique strengths of element specific X-ray imaging techniques from the energy domain into the time domain. The sensitivity of atomic inner shell resonances to the local valence electronic structure makes ultrafast differential CDI an important stepping stone toward the goal of using ultrashort X-ray pulses for real-time imaging of chemical and electronic dynamics with femtosecond time-resolution and nanometer spatial resolution. This capability would open new routes to directly observe chemical and electronic function in complex systems on a molecular scale. For example, it may permit to monitor electronic dynamics in polymer-based electronic devices, the propagation of light-induced reaction fronts in photoresists, or the spatiotemporal distribution of intermediates in catalytic processes.

Acknowledgments

We thank Stefano Marchesini for helpful discussions about the analysis of CDI images and Chris Hahn for generating the SEM image of the sample. This work was supported by Laboratory Directed Research and Development (LDRD) funding from Berkeley Lab, provided by the Director, Office of Science, of the U.S. Department of Energy under Contract No. DE-AC02-05CH11231.

#174995 - $15.00 USD Received 27 Aug 2012; revised 19 Oct 2012; accepted 21 Oct 2012; published 5 Nov 2012